Journal of Membrane Science and Research 8 (2022) 538060

Journal of Membrane Science & Research

journal homepage: www.msrjournal.com

Research Paper

Molecular Mobility of Polynorbornenes with Trimethylsiloxysilyl side groups: Influence of the Polymerization Mechanism

Mohamed Aejaz Kolmangadi [1], Paulina Szymoniak [1], Glen Jacob Smales [1], Maxim Bermeshev [2], Andreas Schönhals [1], Martin Böhning [1,*]

[1] *Bundesanstalt für Materialforschung und -prüfung (BAM), Unter den Eichen 87, 12205 Berlin, Germany*
[2] *A.V. Topchiev Institute of Petrochemical Synthesis of Russian Academy of Science, Moscow, Russia*

Article info

Received 2021-09-14
Revised 2021-11-18
Accepted 2021-11-19
Available online 2021-11-19

Keywords

Microporous polymers
Molecular mobility
Electrical conductivity
Membrane polymers
Gas separation

Highlights

- Metathesis and addition-type polynorbornenes from the same monomer were compared
- Differences in molecular mobility are clearly revealed by Dielectric Spectroscopy
- Dynamic and structure reveal microporous nature of the addition-type polynorbornene
- Conductivity behavior reflects differences in mobility and microporosity
- Characteristics of structure and dynamics are discussed in view of gas transport

Graphical abstract

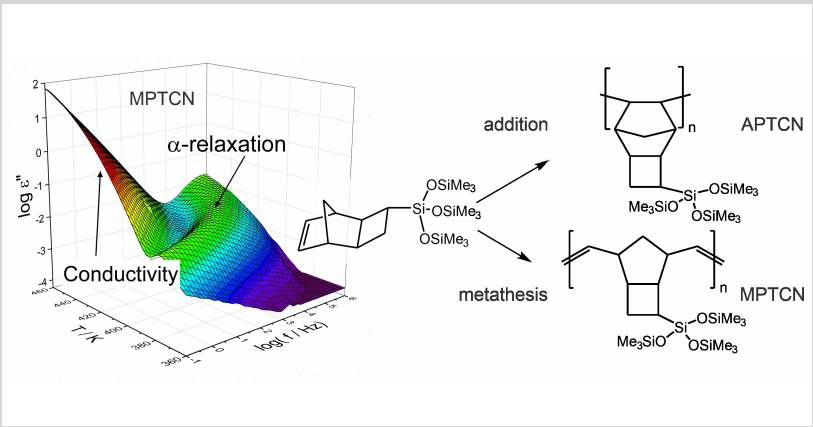

Abstract

We report dielectric and calorimetric studies on metathesis and addition-type polytricyclononenes, both based on the same monomer bearing three pendant $OSiMe_3$ groups. For the addition-type polymer, dielectric spectroscopy reveals a β^*-process related to the microporosity, whereas for its metathesis counterpart, the segmental dynamics manifests as an α-process related to a glass transition. Besides active dielectric processes, a significant conductivity contribution is detected for both samples which for the microporous addition-type polymer is three orders of magnitude greater than for the metathesis polymer. The broadband dielectric spectroscopy is complemented by detailed calorimetric investigations, comprising DSC, FSC, and TMDSC. The calorimetric methods detected the glass transition for the metathesis polymer in agreement with the observed dielectric α-process. Furthermore, the already reported gas transport properties for both polymers are compared, setting them in correlation with the observed molecular mobility and conductivity behavior. The discussed results reflect significant differences in molecular mobility of the two polymers affecting the appearance of microporosity which strongly determines the gas transport properties.

© 2022 FIMTEC & MPRL. All rights reserved.

1. Introduction

Membrane technology is continually emerging as a promising alternative to conventional gas separation techniques proving to be cost and energy efficient whilst also being environmentally friendly [1,2,3]. Besides industrial operations and the treatment of natural gas, membrane technology will also play a decisive role in the context of renewable energy supplies. It is already in use for biogas upgrading and is currently under discussion for the separation of "green" hydrogen when distributed in existing gas grids. Here, the scalability of this technology is of great advantage, allowing for large membrane plants as well as for distributed local installations – all based on the same modules. The application of polymers as active separation layers in gas separation membranes is well established due to the ease of processing by casting or coating from solution.

The development and further optimization of polymers for gas separation membranes has been an ongoing task in academic as well as industrial research for several decades. These continuous efforts historically lead from rubbery polymers, such as poly(dimethyl siloxane) (PDMS), to conventional glassy polymers, such as polysulfone, with lower permeabilities but significantly higher permselectivities. As a result of further developments, higher permeabilities have been obtained for glassy polyimides with considerably larger fractional free volume due to stiffer backbone structures which in turn gave rise to higher glass transition temperatures. This class of polymers already stands out due to its versatile chemistry and with ongoing research producing many different polymer structures with some even being transferred to large-scale industrial membrane applications [4].

* Corresponding author: martin.boehning@bam.de (M. Böhning)

DOI: 10.22079/JMSR.2021.538060.1495

Another outstanding development was the emergence of polyacetylenes, i.e., poly(4-methyl-2-pentyne) (PMP) and polytrimethylsilylpropyne (PTMSP), the latter being still one of the most permeable polymers. The double bond in the backbone structure of these polymers results in an extremely loose packing in the solid-state and, hence, these polymers possess an extremely high free volume of these polymers. The downside of the high free volume is the lack of stability of these materials, especially with their strong tendency for physical ageing which is accompanied by a significant loss of permeability and potential membrane performance. This is also one of the most important issues for two further classes of polymers that stimulated the field in recent years. The first, polymers of intrinsic microporosity (PIMs), discovered by Budd and McKeown in 2004 [5,6], are attractive for their separation properties. These are due to a rigid and contorted backbone structure [7] that prevents effective chain packing in the solid-state giving rise to an extremely large fractional free volume and even significant microporosity (as indicated by their BET surface areas of up to 1000 m^2/g) [8]. This results in extremely high gas permeabilities in combination with good selectivities, making them potentially very attractive as membrane materials. Again, similar to polyimides, the chemistry behind PIMs allows for a great variety of structures, giving rise to numerous research efforts and expanding possible applications to other fields such as catalysis, sensor technology, or electrochemistry [9].

Another approach to create free volume and microporosity through insufficient packing of the polymer segments is to combine a rigid backbone with bulky side groups. This is for example realized by the second class of materials – polynorbornenes, another toolbox of polymer chemistry [10,11]. This class of high-performance polymers is again characterized by a great versatility of the chemistry with respect to the monomers that is further supplemented by various modes of polymerization – the ring opening metathesis polymerization (ROMP), the addition polymerization (AP) and the recently developed catalytic arene-norbornene annulation (CANAL). The norbornene monomers are readily accessible by cycloaddition. The current state of the art in this field is summarized in two recent reviews [12,13]. Polymers obtained by metathesis polymerization generally exhibit a more flexible backbone and therefore a higher molecular mobility as well as usually lower glass transition temperatures T_g, even though they contain two double bonds per repeat unit in the main chain due to the polymerization reaction. These double bonds do, however, make them also sensitive to oxidation. In contrast to this, the polymers resulting from addition polymerization are more stable and exhibit better mechanical properties. The sequence of sterically demanding repeat units based on bridged six-membered ring structures limits its intrinsic molecular mobility considerably. This sterically induced rigidity results in much higher glass transition temperatures but also hinders efficient packing in the solid-state giving rise to large fractional free volume or even microporosity. In terms of gas transport properties, the addition type polynorbornenes show much higher permeability values compared to their analogous metathesis polymers.

For the further optimization of properties, these sterically demanding bicyclic repeat units pose a challenge: with more or larger substituents attached, the reactivity of the catalytic addition polymerization is often poor. This limitation can be overcome by separating these substituents by a spacer. In the context of norbornene monomers, this can be achieved by including a four-membered ring into the monomer structure which is also accessible by a cycloaddition reaction [12,14]. The obtained poly(tricyclononenes), which still can be considered a special case of polynorbornenes, open-up a wide range of synthetic variations to further improve the gas transport properties.

Among those polynorbornenes, silylated polymers [10] (those bearing silicon atoms in the side substituents such as trimethylsilyl groups $-SiMe_3$ or trimethylsiloxysilyl side groups $-Si(OSiMe_3)_3$), stand out due to their exceptional permeabilities and gas transport properties. Such polymers include addition-type and metathesis poly(trimethylsilylnorbornenes) (PNB) and poly(trimethylsilyltricyclononenes) (PTCN). A common feature for this class of polymers is that they exhibit a solubility-controlled permeation (also termed 'reverse selectivity'), i.e. the permeability coefficient increases with increasing penetrant size of gaseous hydrocarbons [10] which is in contrast to the commonly observed behavior.

Studies that compare the gas transport [15], free volume [10] and molecular properties [16] of addition and metathesis polynorbornenes bearing silicon-based side groups have previously been reported. It was found that the permeability values increase with both, the number of bulky side groups and the presence of flexible linkers such, as Si-O–Si, that link the side groups to the backbone. However, only a few studies have reported molecular mobility investigations of polynorbornenes [17,18,19], whilst investigations comparing the molecular mobility of addition and metathesis polynorbornenes, based on the same monomers, remain unreported. Studies that address molecular mobility are important as the membrane properties of polymers depend strongly on the interplay of gas sorption and diffusion, with the latter being related to the molecular mobility of the polymer segments or its side groups [18,20]. Although high free-volume polymers may represent a special case in this regard, their tendency for physical ageing is another issue determined by the mobility of the polymer matrix [19].

In the present study, Broadband Dielectric Spectroscopy (BDS) was employed to compare the molecular mobility of metathesis and addition-type polytricyclononenes, based on the same monomer bearing trimethylsiloxysilyl groups, $-Si(OSiMe_3)_3$, i.e. trimethylsilyl groups linked via Si-O-Si spacers to the polymer backbone. The addition-type polymer is known to exhibit microporosity resulting in a BET surface area of 390 m^2/g [21], whilst the metathesis polymer exhibits a surface area of only 10 m^2/g [22], i.e. no significant microporosity. The investigation provides a qualitative picture of the microstructure of the polymers that is complemented by the X-ray scattering data.

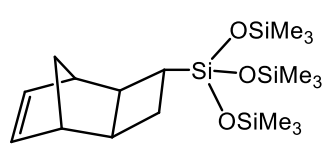

a) Tricyclononene monomer

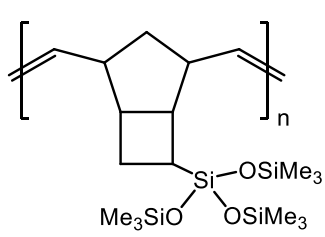

b) Metathesis-type "MPTCN", BET: 10 m^2/g [22]

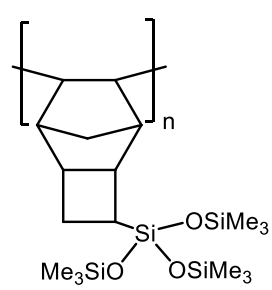

c) Addition-type "APTCN", BET:390 m^2/g [21]

Fig. 1. Chemical structures of the two polytricyclononenes under investigation and the corresponding monomer.

2. Materials and methods

The materials in the present study are polytricyclononenes containing three pendant -$OSiMe_3$ groups connected to a central Si substituent at a four-membered ring of the tricyclononene repeat unit (see Figure 1). Depending on the choice of catalyst, from the same norbornene monomer (here the tricyclononene shown in

Fig. 1.a) two distinctly different polymers can be obtained. Using a Grubbs catalyst based on Ruthenium carbene complexes the metathesis product, shown in

Fig. 1.b, is obtained by ring-opening metathesis polymerization (ROMP). The addition-type polymer (

Fig. 1.c) is formed by opening of the double bond in the presence of a Palladium catalyst. Both routes lead to high molecular weight polymers. Further details concerning the synthesis of the polynorbornenes are reported in ref. [14]. The low frequency vibrational density of states of APTCN as investigated by neutron scattering is addressed elsewhere [23].

2.1. Sample preparation

Polymer films were prepared by dissolving 0.13 g of polymer in 3.5 ml of toluene, followed by shaking for 5h at room temperatures. The solutions were filtered with a 0.2 µm PVDF filter, cast into a Teflon mold of 2.5 cm diameter and then placed inside a closed chamber with saturated toluene vapor at room temperature to control the initial evaporation of the solvent from the film. After three days, the molds were removed from the chamber, and films with a thickness of ca. 120 µm were obtained. Subsequently, the films were dried for 3 days at 393 K in an oven with an oil-free vacuum to ensure a complete removal of the solvent. The obtained films were clear and transparent. X-ray scattering measurements and calorimetric experimentswere carried out directly on the obtained films. For the BDS measurements, aluminum electrodes were deposited on the surface of the films. The deposition of aluminum electrodes of a diameter of 10mm on the film was achieved by physical vapor deposition.

2.2. Broadband dielectric spectroscopy (BDS)

For the dielectric spectroscopy an ALPHA analyzer of Novocontrol (Montabaur, Germany) was employed. The high-resolution device was connected to a sample holder providing an active sample head, working in parallel plate geometry. Nitrogen gas was used as medium for heating and cooling of the sample with a stability < 0.1 K (Quatro cryo-controller of Novocontrol). For the measurement the film sample was placed between circular electrodes of 10 mm diameter made from brass and coated with gold. By frequency scans under isothermal conditions the complex dielectric permittivity $\varepsilon^*(f) = \varepsilon'(f) - i\varepsilon''(f)$ was determined at frequencies ranging from 10^{-1} to 10^{-6} Hz. The temperature range for these measurements was between 133 K and 463 K. In the equation defining the complex dielectric permittivity ε^*, $i = \sqrt{-1}$ represents the imaginary unit, while f corresponds to the frequency, and the real and imaginary part of the complex dielectric function are denoted by ε´ and ε´´. The respective heating/cooling cycles were performed in three subsequent measurement runs.

2.3. Advanced calorimetry

2.3.1. Differential scanning calorimetry

For the DSC measurements a DSC 8500 device of Perkin Elmer (Waltham (MA), USA) was used with 10 K/min as heating and cooling rate in the temperature range of -80 – 190 °C. Corrections of the baseline are based on measurements with empty pans (sample and reference) in the power compensation mode using 20 ml/min nitrogen as purge gas. Indium was used as standard for the calibration of temperature. At least two subsequent heating runs were performed, the data were determined from the second heating run.

2.3.2. Temperature modulated DSC (TMDSC)

The same Perkin Elmer DSC 8500 instrument was employed for TMDSC using the StepScan approach. StepScan DSC (SSDSC, trademark of Perkin Elmer) is a variant of TMDSC: a periodic temperature perturbation is realized by short heating and isothermal steps in alternating sequence. This allows for the determination of the complex heat capacity from the heat flow measured in this manner. The frequency of the temperature modulation is related to the duration of the isothermal step. In this study the frequency range of 10^{-3} to 10^{-2} Hz was used with a step height of 1 K (constant) and a 80 K/min heating rate, purging with N_2 with 20 ml/min.

2.3.3. Fast scanning calorimetry (FSC)

Fast scanning calorimetry is often used to decouple thermal transitions of the investigated material from its thermal degradation by applying extremely fast heating rates [17,24]. Furthermore, the accessible heating rates allow for coverage of a wider range of corresponding characteristic frequencies for the determination of such transitions, e.g., the glass transition of polymers.

The samples in this study were further investigated with respect to their thermal behavior by means of FSC using a Mettler Toledo Flash DSC1. This device is a power compensated DSC [25] allowing for heating rates ranging from 0.5 K/s to 40000 K/s. Twin chip sensors of the MultiSTAR UFS1 type were employed as sample cells, purged with N_2 at 40 ml/min. A TC100 intra-cooler of Huber Kältemaschinenbau AG (Offenburg, Germany) was used for cooling. Prior to the measurement, the recommended procedure of the supplier for conditioning and correction of the sensor was applied. The samples (some 100- 200 ng) were cut down to dimensions in the micrometer range and placed carefully on the sensor area (sample side) of the chip. A silicon oil of high viscosity (AK 60 000 of Wacker Chemie AG, München, Germany) is applied in order to provide good thermal contact of the sample on the sensor and for minimizing thermal lags. For compensation of the additional heat capacity due to the silicon oil, an equal amount was placed on the sensor area of the reference side. Measurements with heating rates up to $30 \cdot 10^3$ K/s and cooling rates up to $7 \cdot 10^3$ K/s were performed in the temperature range of 263 K – 433 K for MPTCN and 298 K - 723 K for APTCN.

2.4. X-ray scattering

X-ray scattering, i.e. small and Wide-angle measurements, were performed employing the "Methodology Optimization for Ultrafine Structure Exploration" (MOUSE), using a highly customized Xeuss 2.0 instrument for SAXS/WAXS by Xenocs (Grenoble, France) [26]. X-ray generation was based on a microfocus X-ray tube with a copper target. To parallelize the beam and monochromatize it to the Cu K_α wavelength of 0.1542 nm a multilayer optic was employed. Data collection was realized by an in-vacuum detector Eiger 1M of Dectris (Baden, Switzerland), placed at multiple distances from the sample (between 52 and 207 mm). For processing of the obtained data the DAWN software package [27,28] has been used according to standardized procedures considering the propagation of errors.

3. Results and discussion

3.1. Dielectric spectroscopy

Figure 2a depicts the 3D representation of dielectric loss as a function of temperature and frequency for MPTCN. One dielectrically active process is observed for this polymer as a distinct peak in the dielectric loss spectra (see Figures 3a and 3b) denoted as α-relaxation. Furthermore, there is a significant conductivity contribution at low frequencies and high temperatures. This contribution is indicated by a linear increase of log ε'' and the result of mobile charge carriers in the polymer matrix. Typically, the concentration of these charge carriers is at the ppm level.

The dielectric relaxation process was analyzed quantitatively by a fit of the Havriliak-Negami (HN) model function to the experimental data. The HN-function reads [29].

$$\varepsilon^*_{HN} = \varepsilon_\infty + \frac{\Delta\varepsilon_{HN}}{(1+(i\omega\tau_{HN})^\beta)^\gamma}. \quad (1)$$

where ε_∞ corresponds to the real part of complex dielectric permittivity ε^* in the limit of $\varepsilon_\infty = \lim_{\omega\to\infty} \varepsilon'(\omega)$. The dielectric strength is denoted by $\Delta\varepsilon_{HN}$ and the relaxation time τ_{HN} is related to the frequency f_{max} of the maximum dielectric loss. The fractional parameters β and γ $(0 < \beta;\ \beta\gamma \leq 1)$ represent the symmetric and asymmetric broadening of the relaxation spectrum according to the model of Debye [30].

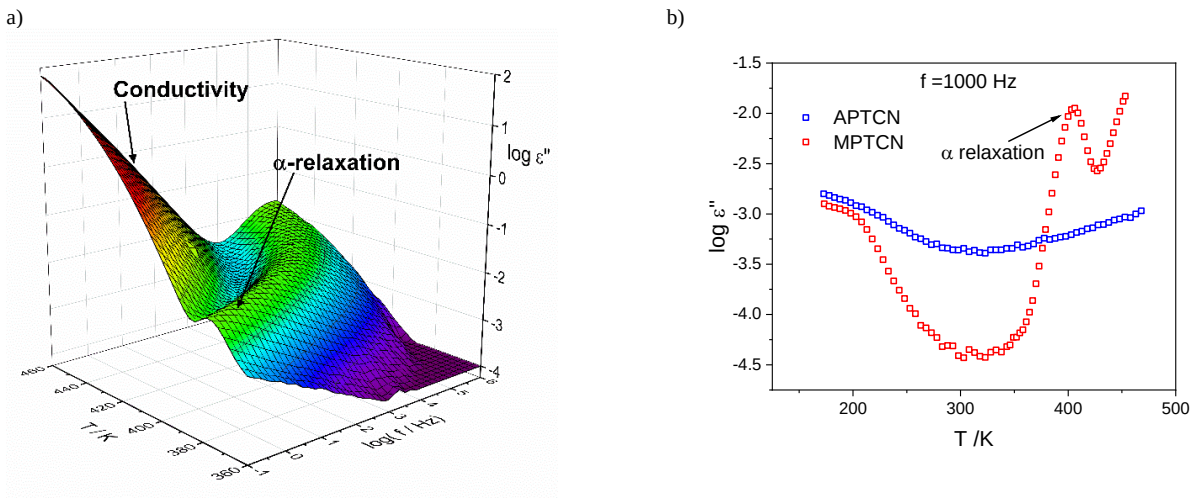

Fig. 2. (a) 3D representation of the dielectric loss as a function of temperature and frequency for MPTCN, (b) Isochronal dielectric loss representation for MPTCN and APTCN at a frequency of 1000 Hz.

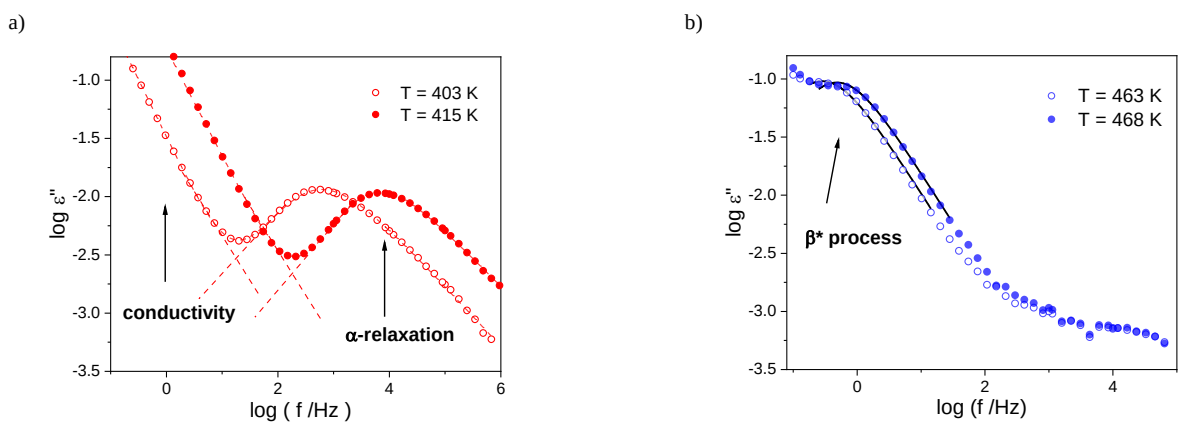

Fig. 3. Frequency dependence of dielectric loss at the indicated temperatures for (a) MPTCN and (b) APTCN. Solid lines are the fits of the HN-function to the data.

Figure 3a shows examples of the HN-fits to the data of α-relaxation of MPTCN. The peak related to the α-relaxation as well as the linear increase at lower frequencies due to electrical conductivity are clearly discernible.

In contrast to MPTCN, APTCN exhibits no dielectric α-relaxation (see Fig. 2.b). Nevertheless, besides the conductivity-related linear increase towards lower frequencies, in the frequency-dependent plot of log e'' (Fig. 3.b) a process is observed indicated as a shoulder at higher temperatures, which is denoted as β*-process. Also, the β*-process of APTCN is analyzed by a HN-fit to the data. The analysis revealed the shape of the β*-process to be more or less Debye-like.

The fitting parameters provide the (relaxation) rate $f_{max,}$ corresponding to the loss peak's maximum position at different temperatures. These rates are plotted in the relaxation map as function of the inverse temperature (see Figure 4). Here, the temperature dependence of the relaxation rate of the β*-process of APTCN is linear and follows an Arrhenius equation given by:

$$f_{max} = f_{\infty} \exp\left[-\frac{E_A}{RT}\right] \quad (2)$$

In equation 2, f_{∞} is the relaxation rate at infinite temperature, E_A is the activation energy and the universal gas constant is denoted R. The activation energy of the β* process of APTCN is determined as 248 kJ/mol and is distinctly higher compared to activation energies of localized processes [31]. Therefore, this β*-process of APTCN is assigned to a Maxwell Wagner Sillars (MWS) polarization (see also refs. [18] and [19]). Such MWS processes, at high temperatures, occur due to the blocking of charge carriers at the walls of micropores [30] and have previously been observed for other silicon-containing addition polynorbornenes [19]. This assignment is consistent, as APTCN is microporous with a BET surface area value of 390 m^2/g.

For MPTCN, the temperature dependence of the relaxation rates of the α process is curved when plotted versus inverse temperature (Figure 4). This behavior is described by the empirical Vogel-Fulcher-Tammann (VFT) equation [32], which reads:

$$\log f_{max} = \log f_{\infty} - \frac{A}{T-T_0} = \log f_{\infty} - \frac{DT_0}{2.3(T-T_0)} \quad (3)$$

f_{∞} is a pre-exponential factor, A is a constant, and T_0 is the so-called Vogel temperature related to an ideal glass transition. For conventional glass forming systems T_0 is usually found 30-70 K below the thermal glass transition temperature. D is known as the fragility parameter or the fragility strength and is used to classify glass forming systems [33]. This VFT-like temperature dependence is a signature of glassy dynamics and therefore the α-relaxation is assigned to the cooperative segmental fluctuations (glassy dynamics) of the MPTCN backbone. Such segmental fluctuations are possible for the more flexible backbone of MPTCN in contrast to that of APTCN where the limited backbone mobility also gives rise to the observed microporosity.

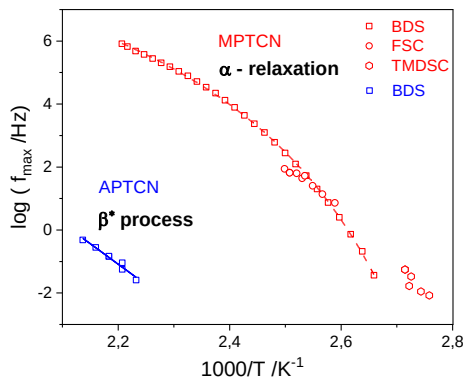

Fig. 4. Relaxation map of MPTCN and APTCN including data obtained from BDS, FSC and TMDSC. Solid and dashed lines represent the fit of the Arrhenius and VFT-equation to the data, respectively.

3.2. Calorimetry

The glass transition temperature (T_g) of MPTCN, related to the α-relaxation process observed in the dielectric spectra, was also investigated by conventional DSC, TMDSC, and FSC. The DSC thermogram for MPTCN is shown in Figure 5a, in which a step-like change corresponding to the glass transition is observed. T_g was estimated as the temperature of the mid-height step as sketched in Figure 5a. For APTCN no glass transition could be observed by DSC before the thermal degradation of the polymer (see Fig. **5**.a). It should be noted that the glass transition of APTCN is expected to be at temperatures close or above its thermal degradation.

TMDSC investigations are shown in Figure 5b. Here, the specific heat capacity cp(T) is plotted versus temperature for different frequencies, i.e. isothermal time steps of different lengths. The dynamic glass transition temperature was obtained by evaluating the mid step position of the heat capacity cp(T) measured at the respective frequency. The obtained dynamic T_g values with their corresponding frequencies are plotted in the relaxation map in comparison with the dielectric data for MPTCN, see Fig. **4**.. Although the absolute values of the TMDSC data (thermal relaxation rates) are slightly different from the BDS data (dielectric relaxation rates), both data sets agree in their temperature dependence. Such shifts have previously been observed for other polynorbornenes [17] as well as other polymers [34].

FSC experiments were carried out on MPTCN by employing fast heating and cooling rates. The FSC thermograms at different heating rates are shown in Figure 6a. Again, characteristic step–like changes corresponding to T_g were observed. The temperature of the half step height was taken to determine the glass transition temperature for each heating rate. The results reflect the expected shift of T_g with increasing heating rate towards higher temperatures due to the kinetic nature of the glass transition. The estimated glass transition temperatures are plotted together with the heating rate in the Arrhenius diagram. As expected, this dependence is curved in that representation as expected for a glass transition (see Fig. **6**.b). For APTCN no glass transition was observed by FSC, in line with the observation from DSC experiments.

a) b)

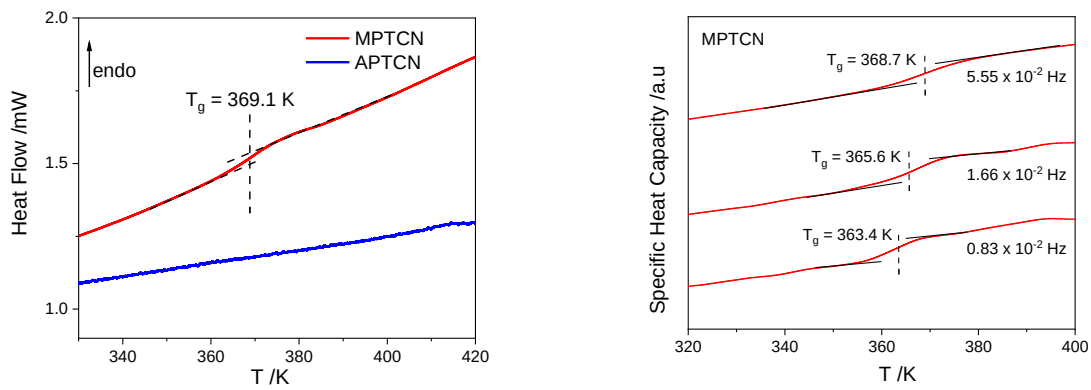

Fig. 5. (a) DSC thermogram for the second heating run at 10 K/min for MPTCN and APTCN. The dashed line indicates the position of the estimated glass transition for MPTCN, (b) Specific heat capacity from TMDSC (step scan) versus temperature at the indicated frequencies for MPTCN. Dashed lines indicate the estimated glass transition temperature. The curves are shifted along the y-axis for the sake of clarity.

a) b)

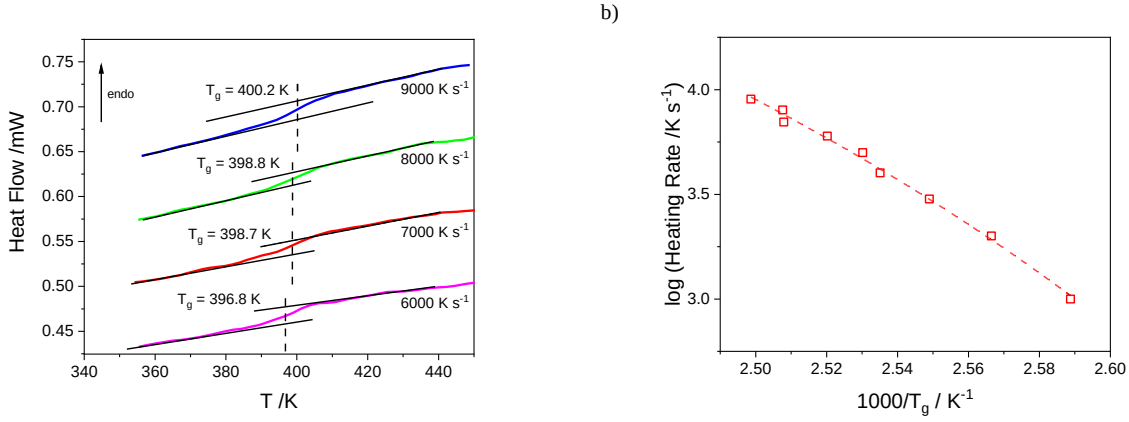

Fig. 6. (a) FSC heating thermograms for MPTCN at the indicated heating rates - dashed lines in the center indicate the estimated glass transition temperatures. (b) Logarithmic heating rate versus inverse T_g for MPTCN. The dashed line is the fit of the VFT-equation.

The frequency dependence of FSC data measured for MTPCN was obtained by converting the heating rates into thermal relaxation rates f_{max} using a relation developed by Donth [35] given by,

$$f_{max} = \frac{\dot{T}}{2\pi a \Delta T_g} \tag{4}$$

Here, $\dot{T}$ is the heating rate, and ΔT_g is the width of the glass transition. a is a constant with a value of approximately one. The temperature dependence of the FSC thermal relaxation rates is curved when plotted versus inverse T_g and follows VFT behavior (see Fig. **4.**). This is also in good agreement with the dielectric values. The glass transition observed by FSC is also assigned to the segmental fluctuations of the MPTCN backbone.

3.3. Structural aspects

The difference of MPTCN and APTCN concerning their microporosities is studied by X-ray scattering. Three peaks (I, II, and III) were observed in the X-ray data for both polymers (Figure 7). The corresponding d-spacing values were calculated using the Bragg-equation $d = \frac{2\pi}{q}$ and are summarized in Table 1. Peak I at low q is most apparent for APTCN and may be assigned to the micropores present in the material as similar peaks have been observed for other polynorbornenes (PTCNSi2g [18], PTCNSi1 [19]). The higher intensity of peak I, observed for APTCN, indicates that these micropores occupy a greater volume fraction within this polymer, which corresponds well with its considerable BET surface area. Interestingly, MPTCN also shows a slight peak in this range although the BET surface area values do not suggest significant microporosity which is expected due to the higher backbone mobility that should lead to more efficient packing in the solid-state. It should be noted that only open pores which are accessible to nitrogen can be observed by the BET method. It might be that MPTCN has some internal, inaccessible pores that are hidden for the BET measurements.

The d-values of the peaks II and III at high q values are similar for MPTCN and APTCN, and comparable to values found in literature (Table 1). Peaks II and III in reference [22] were assigned to the intermolecular and intramolecular correlation of the polymer segments. However, as the d-spacing value of peak III is similar for both MPTCN and APTCN, here peak III is assigned to the backbone correlations of polymer segments, and peak II may be due to the intramolecular correlations in the polymer.

Despite being synthesized from the same monomer, marked differences in the properties of APTCN and MPTCN are observed, due to the differences in both, the structural and conformational parameters of the polymer segments. Yevlampieva et al. [36], performed hydrodynamic and electro-optical studies on metathesis and addition APNBSi. The main chain of the addition polymer belonged to the vinyl group of polymers and that of metathesis polymer belonged to the diene group of polymers. The rigidity of the addition polymer was two orders of magnitude greater in comparison to its metathesis counterpart. It was reported that the metathesis polymers showed stereoregularity in the form of cis conformations, which contributes to the flexible nature of their backbones. The same analogy can be applied in our case, as it is observed that the backbone of APTCN is more rigid than that of MPTCN. In addition, as the bulky trimethylsiloxysilyl side groups are closer in vicinity causing a substantial hindrance of rotational degrees of freedom, there is an increase of the backbone rigidity.

3.4. Conductivity

For both polymers, MPTCN and APTCN, a conductivity contribution was observed at high temperatures and low frequencies. The observed conductivity in both materials may be due to some ionic impurities or traces of catalyst, i.e. mobile charge carriers present in the matrix.

The relation between the complex conductivity σ* and the complex dielectric function ε* is given by

$$\sigma^*(\omega) = \sigma'(\omega) + i\sigma''(\omega) = i\omega\varepsilon_0\varepsilon^*(\omega) \tag{5}$$

Here, ω is the angular frequency ω=2πf, $\sigma'(\omega)$ and $\sigma''(\omega)$ are the real and imaginary part of the complex conductivity given by

$$\sigma'(\omega) = \omega\varepsilon_0\varepsilon''(\omega) \tag{6}$$

and

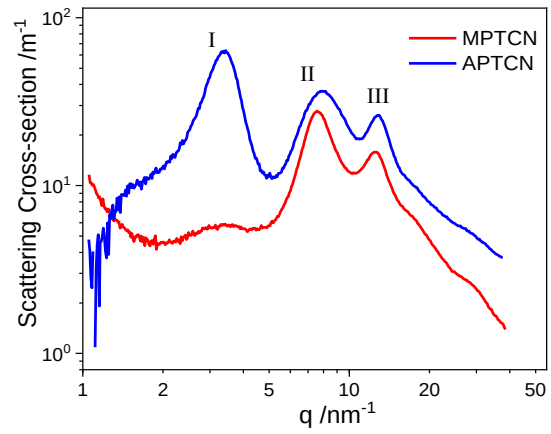

Fig. 7. X-ray scattering pattern for MPTCN and APTCN. Error bars are omitted as they are in the range of the plotted line thickness.

Table 1
d-spacing values for MPTCN and APTCN.

Material	d value /Å		
	Peak I	Peak II	Peak III
APTCN [this study]	18.5	7.8	4.9
MPTCN [this study]	18.2	8.3	5.0
MPTCN (literature values)		8.5 [22]	5.1 [22]

$$\sigma''(\omega) = \omega\varepsilon_0\varepsilon'(\omega) \tag{7}$$

The frequency dependence of the real part of the complex conductivity for MPTCN and APTCN is depicted in Figure 8a. The σ' spectra exhibit three features, (i) a power law behavior at high frequencies down to a characteristic frequency f_c, (ii) a frequency independent plateau-like region at frequencies below f_c corresponding to σ_{DC}, being the DC conductivity, and (iii) a decrease at low frequencies caused by effects of electrode polarization (EP). This electrode polarization occurs due to the blocking of charge carriers at the electrode interface. As a common parasitic effect in dielectric spectra is not considered further here. The frequency dependence of the real part of the complex conductivity σ' was analyzed by the empirical power law of Jonscher [37] (it should be noted that other models based on theoretical approaches exist in the literature [38]).

The Jonscher equation reads as,

$$\sigma'(f) = \sigma_{DC}\left(1 + \left(\frac{f}{f_c}\right)^n\right) \tag{8}$$

where σ_{DC} denotes the DC conductivity, n is an exponent with values between 0 and 1. The relation between DC conductivity and the characteristic frequency f_c is described by the empirical Barton–Nakajima–Namikawa (BNN) relation [38]. In this study the DC conductivity values were obtained by fitting the Jonscher-equation to the data.

As can be seen in Figure 8a, the absolute value of DC conductivity of MPTCN is three orders of magnitude greater in comparison to that of APTCN. Figure 8b depicts the temperature dependence of the DC conductivity versus inverse temperature. The temperature dependence of the DC conductivity for APTCN is linear versus inverse temperature and follows Arrhenius behavior with an activation energy value of EA = 180 kJ/mol, whereas that for MPTCN is clearly curved and obeys the VFT-relation. This implies that the conductivity contribution observed in MPTCN can be correlated with the segmental dynamics of the polymer. This is plausible as it is emerging at temperatures above the glass transition temperature T_g. Though, the same cannot be said for APTCN as the conductivity is observed below the glass transition and is assigned to the propagation of charge carriers through the micropores [18,19].

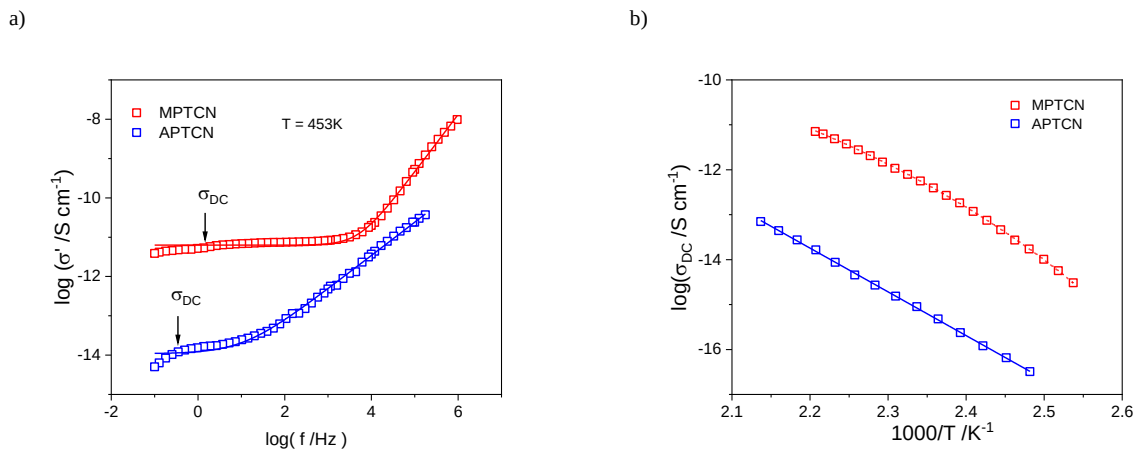

Fig. 8. (a) Frequency dependence of the real part of the complex conductivity at the indicated temperatures. Solid lines are the fits of Jonscher-equation to the corresponding data. (b) DC conductivity versus inverse temperature. Solid and dashed lines are fits it of Arrhenius and VFT-equation to the data, respectively.

3.5. Gas transport properties

A comparison of gas transport properties for MPTCN and APTCN is provided in Table 2 and Table 3. The data were obtained from reference [14]. The permeability of gases in APTCN is on average 5 – 6 times higher than MPTCN. Nevertheless, the MPTCN studied here exhibits higher permeabilities compared to analogous metathesis polynorbornenes with -$SiMe_3$ side groups [12]. The high permeability was attributed to both the presence of the same bulky -$SiMe_3$ side groups that enable loose chain packing and a high free volume but connected in this case by the flexible Si – O – Si linker acting as spacer and promoting the gas transport further. Interestingly, the more than four times higher permeability in this case goes along with only a minimal loss of selectivity [14]. In contrast, with respect to permselectivities of the two polymers under investigation, MPTCN has higher selectivity in comparison to APTCN and follows the Robeson upper bound for most of the gas pairs except for alkanes, where the trend is reversed and APTCN exhibits higher selectivity values. The latter is ascribed to a solubility-controlled selectivity which is often observed for higher hydrocarbons in silicon containing polymers. For the lighter gases the selectivity is due to differences in diffusivity which is more or less coupled to the molecular mobility of the polymer. The distinctly higher permeabilities of the addition-type polymer, APTCN, is clearly a result of its microporosity. It should be noted here that also the conductivity in this polymer is determined by its microporous nature, whereas for the more conventional MPTCN, it is coupled to the segmental mobility of the backbone as revealed by the VFT-like temperature dependence.

Table 2
Permeability values at 20 °C (293 K) of MPTCN and APTCN for the indicated gases. Values are taken from reference [14].

Polymer	*P* /Barrer								
	He	H_2	O_2	N_2	CO_2	CH_4	C_2H_6	C_3H_8	C_4H_{10}
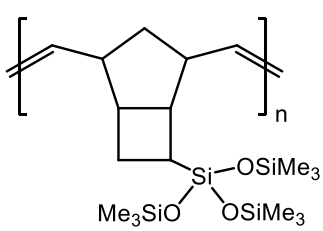 MPTCN	220	360	170	55	830	180	270	290	1940
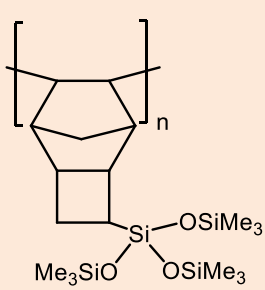 APTCN	1110	2040	960	420	4020	1250	2370	3490	22200

Table 3
Ideal selectivity values at 20 °C (293 K) for MPTCN and APTCN. Values are taken from reference [14].

Polymer	Ideal gas separation selectivity								
	O_2/N_2	H_2/N_2	CO_2/N_2	CO_2/CH_4	H_2/CH_4	He/N_2	C_2/C_1	C_3/C_1	C_4/C_1
MPTCN	3.1	6.5	15.1	4.6	2.0	4.0	1.5	1.6	10.8
APTCN	2.3	4.9	9.6	3.2	1.6	2.6	1.9	2.8	17.8

4. Conclusion

To summarize, we investigated the molecular mobility of metathesis and addition polynorbornenes bearing pendant trimethylsiloxysilyl side groups. The dielectric dispersion revealed the segmental dynamics for the metathesis backbone for MPTCN and a MWS polarization process for APTCN, related to the blocking of charge carriers at the interface of micropores in the polymer. The calorimetric investigation detected a thermal glass transition for MPTCN, the polymer with the backbone derived by metathesis polymerisation which agrees with the dielectric α- relaxation, while no glass transition was detected for APTCN by DSC and FSC as its thermal glass transition temperature is close to its thermal degradation temperature. The absolute value of DC conductivity for MPTCN is three orders of magnitude higher than for APTCN which is due to higher mobility and flexible structure (in spite of the presence of two double bonds) of MPTCN. X-ray scattering experiments show that there is some rudimental microporosity in MPTCN, despite its low BET value, while APTCN is thoroughly microporous. As for the gas transport properties, both MPTCN and APTCN have comparable permselectivities, despite a strong difference in permeability due to their different microporosity as reflected by the corresponding BET surface area values, we associate this behavior with the high mobility of MPTCN segments.

Acknowledgement

We dedicate this paper to the memory of Professor Yuri Yampolskii – one of the most influential researchers in the field of polymer membranes in the last decades.

References

[1] P. Bernardo, E. Drioli, G. Golemme, Membrane Gas Separation: A Review/State of the Art. *Ind. Eng. Chem. Res.* 48 (2009) 4638-4663, DOI: 10.1021/ie8019032

[2] Y. Yampolskii, Polymeric Gas Separation Membranes. *Macromolecules* 45 (2012) 3298-3311, DOI: 10.1021/ma300213b

[3]. Z.-X. Low, P.M. Budd, N.B. McKeown, D.A. Patterson, Gas Permeation Properties, Physical Aging, and Its Mitigation in High Free Volume Glassy Polymers. *Chem. Rev.* 118 (2018) 5871–5911, DOI: 10.1021/acs.chemrev.7b00629

[4]. Sepuran green membranes by Evonik; https://www.membrane-separation.com/en (accessed 2021 -07 -29).

[5]. P.M. Budd, B.S. Ghanem, S. Makhseed, N.B. McKeown, K.J. Msayib, C.E.Tattershall, Polymers of Intrinsic Microporosity (PIMs): Robust, Solution-Processable, Organic Nanoporous Materials. *Chem. Commun.* (Cambridge, U. K.) (2004) 230−231, DOI: 10.1039/b311764b

[6]. P.M. Budd, K.J. Msayib, C.E. Tattershall, B.S. Ghanem, K.J. Reynolds, N.B. McKeown, D. Fritsch, Gas Separation Membranes from Polymers of Intrinsic Microporosity. *J. Membr. Sci.* 251 (2005) 263−269, DOI: 10.1016/j.memsci.2005.01.009

[7]. N.B. McKeown, P.M. Budd, Exploitation of Intrinsic Microporosity in Polymer-Based Materials. *Macromolecules* 43 (2010) 5163–5176, DOI: 10.1021/ma1006396

[8]. N.B. McKeown, P.M. Budd, Polymers of Intrinsic Microporosity (PIMs): Organic Materials for Membrane Separations, Heterogeneous Catalysis and Hydrogen Storage. *Chem. Soc. Rev.* 35 (2006) 675–683, DOI: 10.1039/b600349d

[9]. M. Carta, R. Malpass-Evans, M. Croad, Y. Rogan, J.C. Jansen, P. Bernardo, F. Bazzarelli, N.B. McKeown, An Efficient Polymer Molecular Sieve for Membrane Gas Separations. *Science* 339 (2013) 303–307, DOI: 10.1126/science.1228032

[10]. E. Finkelshtein, M. Gringolts, M. Bermeshev, P. Chapala, Y. Rogan, Polynorbornenes, in: Y. Yampolskii, E. Finkelshtein (Eds.), Membrane Materials for Gas and Vapor Separation, John Wiley & Sons, Chichester 2017; pp 143–221.

[11]. P.P. Chapala, M.V. Bermeshev, L.E. Starannikova, N.A. Belov, V.E. Ryzhikh, V.P. Shantarovich, V.G. Lakhtin, N.N. Gavrilova, Y.P. Yampolskii, E.Sh. Finkelshtein, A Novel, Highly Gas-Permeable Polymer Representing a New Class of Silicon-Containing Polynorbornens As Efficient Membrane Materials. *Macromolecules* 48 (2015) 8055–8061, DOI: 10.1021/acs.macromol.5b02087

[12] X. Wang, T.J. Wilson, D. Alentiev, M. Gringolts, E. Finkelshtein, M.V. Bermeshev, B.K. Long, Substituted polynorbornene membranes: a modular template for targeted gas separations. *Polym. Chem.* 12 (2021) 2947-2977, DOI: 10.1039/D1PY00278C

[13] D.A. Alentiev, M.V. Bermeshev, Design and Synthesis of Porous Organic Polymeric Materials from Norbornene Derivatives. *Polym. Rev.* (Philadelphia, PA, U. S.) (2021), DOI: 10.1080/15583724.2021.1933026

[14]. M.V. Bermeshev, A.V. Syromolotov, M.L. Gringolts, L.E. Starannikova, Y.P. Yampolskii, E. Sh. Finkelshtein, Synthesis of High Molecular Weight Poly[3-{tris(trimethylsiloxy)silyl}tricyclononenes-7] and Their Gas Permeation Properties. *Macromolecules* 44 (2011) 6637–6640, 10.1021/ma201486d

[15]. M. Gringolts, M. Bermeshev, Y. Yampolskii, L. Starannikova, V. Shantarovich, E. Finkelshtein, New High Permeable Addition Poly(tricyclononenes) with $Si(CH_3)_3$ Side Groups. Synthesis, Gas Permeation Parameters, and Free Volume. *Macromolecules* 43 (2010) 7165–7172, DOI: 10.1021/ma100656e

[16]. N.P. Yevlampieva, M.V. Bermeshev, A.S. Gubarev, P.P. Chapala, M.A. Antipov, Additive Poly[3-(trimethylsilyl)tricyclononene-7]: Molecular Properties and Chain Rigidity. *Polym. Sci. Ser. A* 58 (2016) 324–335, DOI: 10.1134/s0965545x1603007x

[17]. M.A. Kolmangadi, P. Szymoniak, G.J. Smales, D.A. Alentiev, M.V. Bermeshev, M. Böhning, A. Schönhals, Molecular Dynamics of Janus Polynorbornenes: Glass Transitions and Nanophase Separation. *Macromolecules* 53 (2020) 7410-7419, DOI: 10.1021/acs.macromol.0c01450

[18]. H. Yin, P. Chapala, M. Bermeshev, A. Schönhals, M. Böhning, Molecular Mobility and Physical Aging of a Highly Permeable Glassy Polynorbornene as Revealed by Dielectric Spectroscopy. *ACS Macro Lett.* 6 (2017) 813–818, DOI: 10.1021/acsmacrolett.7b00456

[19]. H. Yin, P. Chapala, M. Bermeshev, B.R. Pauw, A. Schönhals, M. Böhning, Influence of Trimethylsilyl Side Groups on the Molecular Mobility and Charge Transport in Highly Permeable Glassy Polynorbornenes. *ACS Appl. Polym. Mater.* 1 (2019) 844–855, DOI: 10.1021/acsapm.9b00092

[20]. M. Böhning, N. Hao, A. Schönhals, Correlation of Activation Energies of Gas Diffusivity and Local Matrix Mobility in Polycarbonate/POSS Nanocomposites. *J. Polym. Sci. Part B: Polym. Phys.* 51 (2013) 1593–1597, DOI: 10.1002/polb.23381

[21]. P.P. Chapala, M.V. Bermeshev, N.N. Gavrilova, Microporous Structure of Highly Permeable Additive Silicon-Containing Polytricyclononenes. *Polym. Sci. Ser. A* 59 (2017) 143–148, DOI: 10.1134/s0965545x17010035

[22]. P. Chapala, M. Bermeshev, L. Starannikova, I. Borisov, V. Shantarovich, V. Lakhtin,V. Volkov, E. Finkelshtein, Synthesis and Gas-Transport Properties of Metathesis Polytricyclononenes Bearing Three Me_3Si Groups per Monomer Unit. *Macromol. Chem. Phys.* 217 (2016) 1966–1976, DOI: 10.1002/macp.201600232

[23]. R. Zorn, P. Szymoniak, M.A. Kolmangadi, M. Wolf, D.A. Alentiev, M. Bermeshev, M. Böhning, A. Schönhals, Low frequency vibrational density of state of highly permeable super glassy polynorbornenes – the Boson peak. *Phys. Chem. Chem. Phys.* 22 (2020) 18381-18387, DOI: 10.1039/D0CP03360J

[24]. H. Yin, Y.Z. Chua, B. Yang, C. Schick, W.J. Harrison, P.M. Budd, M. Böhning, A. Schönhals, First Clear-Cut Experimental Evidence of a Glass Transition in a Polymer with Intrinsic Microporosity: PIM-1, J. Phys. Chem. Lett. 9 (2018) 2003-2008; DOI: 10.1021/acs.jpclett.8b00422

[25]. V. Mathot, M. Pyda, T. Pijpers, G. Vanden Poel, E. van de Kerkhof, S. van Herwaarden, F. van Herwaarden, A. Leenaers, The Flash DSC 1, a Power Compensation Twin-Type, Chip-Based Fast Scanning Calorimeter (FSC): First Findings on Polymers. *Thermochimica Acta* 522 (2011) 36–45, DOI: 10.1016/j.tca.2011.02.031

[26]. G.J. Smales, B.R. Pauw, The MOUSE project: a meticulous approach for obtaining traceable, wide-range X-ray scattering information. *J. Instr.* 16 (2021) P06034, DOI: 10.1088/1748-0221/16/06/P06034

[27]. J. Filik, A.W. Ashton, P.C.Y. Chang, P.A. Chater, S.J. Day, M. Drakopoulos, M.W. Gerring, M.L. Hart, O.V. Magdysyuk, S. Michalik, A. Smith, C.C. Tang, N.J. Terrill, M.T. Wharmby, H. Wilhelm, Processing Two-Dimensional X-Ray Diffraction and Small-

Angle Scattering Data in DAWN 2. *J. Appl. Crystallogr*. 50 (2017) 959–966, DOI: 10.1107/S1600576717004708

[28]. B.R. Pauw, A.J. Smith, T. Snow, N.J. Terrill, A.F. Thünemann, The Modular Small-Angle X-Ray Scattering Data Correction Sequence. *J. Appl. Crystallogr*. 50 (2017) 1800–1811, DOI: 10.1107/S1600576717015096

[29]. S. Havriliak, S. Negami, A Complex Plane Analysis of α-Dispersions in Some Polymer Systems. *J. Polym. Sci. Part C: Polym. Symp.* 14 (1966) 99–117, DOI: 10.1002/polc.5070140111

[30]. A. Schönhals, F. Kremer, Analysis of Dielectric Spectra. in: F. Kremer, A. Schönhals (Eds.), Broadband Dielectric Spectroscopy; Springer, Berlin, Heidelberg, 2003; pp 59–98, DOI: 10.1007/978-3-642-56120-7

[31]. A. Schönhals, Molecular Dynamics in Polymer Model Systems. in: F. Kremer, A. Schönhals (Eds.), Broadband Dielectric Spectroscopy; Springer, Berlin, Heidelberg, 2003; pp 225–293. DOI: 10.1007/978-3-642-56120-7

[32]. A. Schönhals, F. Kremer, The Scaling of the Dynamics of Glasses and Supercooled Liquids. in: F. Kremer, A. Schönhals (Eds.), Broadband Dielectric Spectroscopy; Springer, Berlin, Heidelberg, 2003; pp 99–129, DOI: 10.1007/978-3-642-56120-7

[33]. C.A. Angell, Entropy and Fragility in Supercooling Liquids. *J. Res. Natl. Inst. Stand. Technol.* 102 (1997) 171–185, DOI: 10.6028/jres.102.013

[34]. A. Schönhals, F. Kremer, Amorphous polymers, in: K. Matyjaszewski, M. Möller (Eds.), Polymer Science: A Comprehensive Reference, Vol 1, Elsevier, Amsterdam 2012, pp. 201–226

[35]. E. Donth, The Size of Cooperatively Rearranging Regions at the Glass Transition. *J. Non. Cryst. Solids* 53 (1982) 325–330, DOI: 10.1016/0022-3093(82)90089-8

[36]. N.P. Yevlampieva, M.L. Gringol'ts, I.I. Zaitseva, E.I. Ryumtsev, Molecular Properties of Silicon-Substituted Polymers for Gas-Separation Membranes. *Polym. Sci. Ser. C* 52 (2010) 83–92, DOI: 10.1134/S1811238210010108

[37]. A.K. Jonscher, The 'Universal' Dielectric Response. *Nature* 267 (1977) 673–679, DOI: 10.1038/267673a0

[38]. J.C. Dyre, T.B. Schrøder, Universality of AC Conduction in Disordered Solids. *Rev. Mod. Phys.* 72 (2000) 873–892, DOI: 10.1103/RevModPhys.72.873